A STUDY OF Se–Te–Sn GLASSES BASED ON ADVANCED KINETICS MODELLING AND MODULATED DSC

A.A. JORAID[a,] , A.A. ABU-SEHLY[b], M. ABU EL-OYOUN[a,b],
A.H. MOHAMED[a,c]
[a]*Department of Physics, Taibah University, Madinah, Saudi Arabia.*
[b]*Department of Physics, Assiut University, Assiut, Egypt.*
[c]*Department of Physics, Faculty of Science, Beni-Suef University, Beni-Suef, Egypt.*

The modulated differential scanning calorimetry study of amorphous $Se_{90-x}Te_{10}Sn_x$ (x = 0, 2.5, 5, 7.5, and 10) is reported. The glass samples were fabricated using a conventional melt-quenching method. The processing of the non-isothermal data was performed using the advanced thermokinetics software package. To determine the variation of the activation energy for crystallisation as a function of reaction progress the main three isoconversional methods, namely the differential method of Friedman and the integral methods of Ozawa-Flynn-Wall and Vyazovkin, were used. Based on an ASTM E698 analysis of the data, the effect of Sn content was determined. The Avrami exponent of $Se_{90-x}Te_{10}Sn_x$ was determined and found to be dependent on the Sn content, indicating different dimensions of growth. The prediction of the isothermal reaction progress was employed to calculate the reaction model, $g(\alpha)$. A very large increase in the specific heat values of $Se_{90-x}Te_{10}Sn_x$ was observed at the respective glass transition temperatures, which were also found to be highly Sn-content dependent. The Raman spectra for $Se_{90-x}Te_{10}Sn_x$ together with X-ray diffraction and possible glass structures are discussed. A remarkable change occurs at a Sn concentration of 10 at%, which indicates the formation of $SnSe_2$.

1. Introduction

Modulated differential scanning calorimetry (MDSC) is a form of conventional DSC in which a small oscillation is superimposed upon the otherwise linear heating rate. The technique of modulated differential scanning calorimetry enables the deconvolution of the resultant heat flow profile during this cyclic heating that not only provides the total heat flow obtained from conventional DSC but also separates the total heat flow into its heat capacity-related (reversible) and kinetic (non-reversible) components [1,2].
Chalcogenide glasses are attractive materials due to their various scientific and technological applications. The three chalcogenides with S, Se, and Te as parent elements are the subject of a broad range of scientific research. Selenium and its alloys have become materials of considerable commercial importance in device technology. Although pure Se exhibits a short lifetime, low sensitivity, and high viscosity [3], by alloying selenium with another element, such as tellurium, these difficulties can be overcome, enabling the achievement of higher sensitivity, greater hardness, higher crystallisation temperature, and smaller ageing effects compared with pure Se [4-7]. The substitution of Te for Se partly breaks up the Se_8 ring structure and increases the chain fraction but reduces the chain length of the Te structure, leading to thermal instability. However, the addition of a third element may be used to overcome this negative aspect.

---

*Corresponding author: aaljoraid@taibahu.edu.sa

Thus, the insertion of an impurity, such as Sn, in a Se-Te binary alloy is of particular interest, as such doping of Se-Te alloys has been shown to produce remarkable changes in their properties, such as a higher glass transition temperature, a higher crystallisation temperature, and improved thermal stability compared with the host Se-Te alloy [5-7]. Due to the anticipated advantages, a thermal analysis study of amorphous $Se_{90-x}Te_{10}Sn_x$ (x = 0, 2.5, 5, 7.5, and 10) was performed using modulated DSC. From the non-isothermal results, the activation energies for crystallisation were calculated using AKTS-Thermokinetics software [8]. Additionally, from the reverse heat flow data, the heat capacity was determined. The obtained results are discussed in the framework of Raman spectroscopy and X-ray diffraction (XRD).

2. Experimental methods

2.1 Materials and techniques

The materials in a glassy state were prepared by the well known melt quench technique. High purity elements (99.999% Sigma Aldrich) of Se, Te, and Sn in the proper atomic wt% proportions were sealed in an evacuated (10^{-4} Torr) quartz ampoule (12 mm diameter). The contents were heated to around 950 K for 24 h. The ampoule was regularly shaken to ensure good homogeneity. The melt was quenched in ice water.

The MDSC experiments presented in this paper were performed using a TA Instruments Q-2000 instrument, with an accuracy of $\pm0.1\,^{O}C$ and a sensitivity of 0.2 µW, under dry nitrogen supplied at a rate of 50 ml min^{-1}. To minimise the temperature gradients, a small weight (5 mg) and uniform fine powder from the samples was spread as thinly as possible and encapsulated in standard aluminium sample pans. The samples were initially equilibrated at $20\,^{O}C$ for 2 min, and the non-isothermal MDSC curves were obtained at certain heating rates between 3 and 30 K min^{-1} and with a modulation amplitude of $\pm3\,^{O}C$ and modulation period of 10 s. The temperature and enthalpy calibrations were validated using indium (T_m = 429.75 K, ΔH_m = 28.55 Jg^{-1}) as a standard material.

Raman spectra were measured using a Raman microscope spectrometer (Bruker Senterra RMS System) with a resolution of 3 cm^{-1} at a wavelength of 532 nm at room temperature. The temperature-dependent XRD measurements were performed inside an Anton Paar furnace attached to the diffractometer using CuK_{α} radiation (λ = 1.5418 Å). The X-ray tube voltage and current were 40 kV and 30 mA, respectively.

2.2 Kinetic analysis

The advanced thermokinetics software package AKTS-Thermokinetics was used in this study. Note that the kinetic parameters of the reaction can be significantly influenced by the baseline determination. However, throughout the determination of the thermokinetic parameter the AKTS software tool is able of executing the baseline optimisation simultaneously, thereby increasing the accuracy of the estimated parameters [8]. The software suite is based on isoconversional principle techniques, indicating that the reaction rate at a constant reaction progress α is only a function of temperature.

In solid-state transformations, the kinetic model equation for a single-step process is given by[9,10]:

$$\frac{d\alpha}{dt} = K(T)f(\alpha), \tag{1}$$

where T is the temperature, t is the time, $K(T)$ is the effective overall reaction rate constant, α is the reaction progress (conversion fraction) that represents the volume of the crystallised fraction, and $f(\alpha)$ is the reaction model. Because the reaction rate constant follows the Arrhenius equation, Eq. (1) becomes:

$$\frac{d\alpha}{dt} = A \exp\left(-\frac{E}{RT}\right) f(\alpha), \tag{2}$$

where $A\left(s^{-1}\right)$ is the frequency (pre-exponential) factor, $E\left(kJ\,mol^{-1}\right)$ is the activation energy, and R is the universal gas constant. Under non-isothermal conditions where the reaction rate constant $\beta\left(K\,min^{-1}\right)$ is given by $\left(\beta = dT/dt\right)$, Eq. (2) becomes[9]:

$$\frac{d\alpha}{dT} = \frac{d\alpha}{dt}\left(\frac{1}{\beta}\right) = \frac{A}{\beta} \exp\left(-\frac{E}{RT}\right) f(\alpha), \tag{3}$$

The isoconversional method is a useful method to obtain trustworthy kinetic information for both non-isothermal and isothermal processes. Generally, this method can be divided into two categories: differential and integral methods. However, there are three major isoconversional methods that are commonly used:
- Differential (Friedman)[11]
- Integral (Ozawa-Flynn-Wall)[12,13]
- Integral and Advanced integral based on a non-linear procedure (Vyazovkin) [9,10,14-16]

For different heating rates, β_i, and at a specific reaction progress, α, the Friedman method [11] can be used directly from Eq. (2) as:

$$\ln\left(\frac{d\alpha}{dt}\right)_{\alpha i} = \ln\left(A_\alpha f(\alpha)\right) - \frac{E_\alpha}{RT_{\alpha i}} \tag{4}$$

At this precise value of α the parameters E_α and $\ln\left(A_\alpha f(\alpha)\right)$ are then calculated from a plot of $\ln\left(d\alpha/dt\right)_{\alpha i}$ versus $1/T_{\alpha i}$. The index i represents various temperature programs.

Integrating Eq. (3) leads to:

$$g(\alpha) \equiv \int_{\alpha=0}^{\alpha} \frac{d\alpha}{f(\alpha)} = \frac{A}{\beta} \int_{T_0}^{T_a} \exp\left(-\frac{E}{RT(t)}\right) dT, \tag{5}$$

where $g(\alpha)$ is the integral form of the reaction model. The integral in Eq. (5) does not have an analytical solution, hence a number of approximate solutions exist. Several of these approximate solutions enable the integrals to be solved with very high accuracy.

Ozawa and Flynn and Wall (FWO) each independently developed a method for the determination of the activation energy, which is the so-called integral isoconversional method. This method is based on several curves measured at different, but constant, heating rates. The lower limit of integration gets a value of $T_0 = 0$ if T_0 lies below the temperature at which the reaction rate is visible. The logarithm form of Eq. (5) after integration then becomes:

$$\ln\left(g(\alpha)\right) = \ln\left(\frac{AE}{R}\right) - \ln(\beta) + \ln\left(P(z)\right), \tag{6}$$

where:

$$P(z) = \frac{\exp(-z)}{z} - \int_{-\infty}^{z} \frac{\exp(-z)}{z} \, dz \quad \text{and} \quad z = \frac{E}{RT}. \tag{7}$$

According to Doyle's approximation $\left(\ln P(z) = -5.3305 - 1.0518 \times z\right)$, Eq. (6) becomes [9,10,17]:

$$\ln\left(\beta_i\right)=\ln\left(\frac{AE_\alpha}{R}\right)-\ln\left(g\left(\alpha\right)\right)-5.3305-1.0518\frac{E_\alpha}{RT_{\alpha i}} \ . \tag{8}$$

As a result, from the above equation, the parameter E_α at a specific value of α can be estimated from a plot of $\ln\beta$ versus $1/T_{\alpha i}$.

The third way of determining the activation energy E_α at any particular value of α, can be achieved by using the integral isoconversional method developed by Vyazovkin [9,14-16]. For a series of n experimental runs at different heating rates, the value of E_α that minimises the objective function Ω, is:

$$\Omega=\sum_{i=1}^{n}\sum_{j\neq i}^{n}\frac{I\left(E_\alpha,T_{\alpha i}\right)\beta_j}{I\left(E_\alpha,T_{\alpha j}\right)\beta_i} \ , \tag{9}$$

where the temperature integral, I, can be evaluated as:

$$I\left(E_\alpha,T_\alpha\right)=\int_0^{T_\alpha}\exp\left(\frac{-E}{RT}\right)dT \ , \tag{10}$$

This temperature integral assumed that the value of E_α is constant through the whole of integration. Actually, this assumption introduces a large error if E_α varies strongly with α. This error is eliminated by performing integration over small ranges of the degree of conversion, $\Delta\alpha$, and respectively temperature. Hence, the the temperature integral, I, can be given as:

$$I\left(E_\alpha,T_\alpha\right)=\int_{T_\alpha-\Delta\alpha}^{T_\alpha}\exp\left(\frac{-E}{RT}\right)dT \ , \tag{11}$$

This integral is called advanced temperature integral. We will refer to the Vyazovkin minimization methods as Vyazovkin minimization (Vya) for applying Eq. 10 and advanced Vyazovkin minimization (ad-Vya) for applying Eq. 11, respectively.

Finally, ASTM E698 analysis is a notable method based on the isoconversional principle [18,19]. The hypothesis that the ASTM E698 method based on is that the maximum of the DSC curve of a single-step reaction is reached at the same conversion degree independent of the heating rate. In this method, the slope of the straight line in the plot of the logarithm of the heating rate against the reciprocal of the temperature of the maximum is proportional to the activation energy, just as in the Ozawa-Flynn-Wall analysis. Thus, according to ASTM E698, the activation energy is given as:

$$E=-\frac{R}{1.052}\left[\frac{d\ln\left(\beta\right)}{d\left(1/T\right)}\right] \tag{12}$$

2.3 Heat capacity analysis

In modulated DSC, the total heat flow $\left(dQ/dt\right)$ can be separated into the sum of two components. The first term is the thermodynamic component or reversible heat flow, which is mass and specific heat capacity, $\left(m\ c_p\right)$, and heating rate $\left(dT/dt\right)$ dependent. The second term

is the kinetic component or non-reversible heat flow, which is time and temperature dependent, $f\left(T,t\right)$. The equation that describes heat flow in modulated DSC is [1,20,21]:

$$\frac{\mathrm{d}Q}{\mathrm{d}t}=m\ c_{\mathrm{P}}\ \frac{\mathrm{d}T}{\mathrm{d}t}+f\left(T,t\right)=m\ c_{\mathrm{P}}\ \beta+\Delta H\ \frac{\mathrm{d}\alpha}{\mathrm{d}t},\tag{13}$$

where ΔH is the specific enthalpy of a thermal event. The MDSC apparatus uses two simultaneous heating rates: 1) the average heating rate, which provides total heat flow data that are equivalent to those provided by standard DSC at the same average heating rate, and 2) the modulated heating rate, which is used to obtain heat capacity information at the same time as the heat flow. The heat capacity component in Eq. (13) can be calculated as:

$$m\ c_{\mathrm{P}}=\frac{\mathrm{d}Q/\mathrm{d}t}{\mathrm{d}T/\mathrm{d}t}=\frac{\text{Reversing heat flow}}{\text{Average heating rate }(\beta)},\tag{14}$$

3. Results and discussion

3.1 Kinetics studies

Typical DSC curves obtained at a constant rate of 5 K min^{-1} are shown in Fig. 1. This figure reveals two characteristic peaks for all of the DSC thermograms.
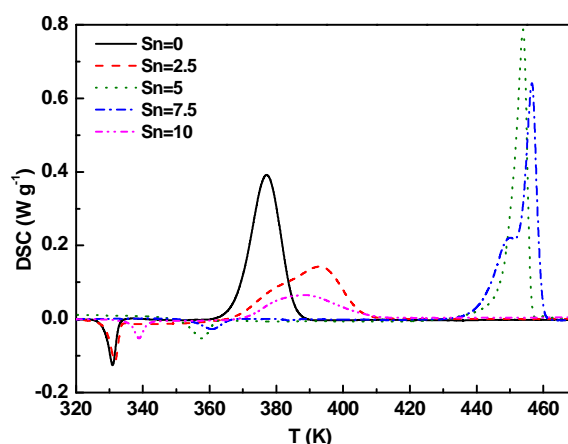

Fig. 1. Typical DSC trace of the chalcogenide Se$_{90-x}$Te$_{10}$Sn$_x$ heated at a constant rate of 5 K min^{-1}.

The first endothermic peak indicates the glass transition region, which arises due to a rapid increase in the specific heat of the sample. The second exothermic peak arises upon crystallisation of the sample. Similar DSC thermograms were observed for the other heating rates. As evident from Fig. 1, the glass transition temperature, T_{g}, and the peak temperature, T_{p}, initially increase with increasing Sn concentration between 0 and 7.5 at%, followed by a sudden decrease when the Sn concentration exceeds 10 at%. The increase in T_{g}, with Sn concentration has been recognized by other workers; the reason may do to that the additions of Sn to the weaker bond of Se-Se are replaced by the stronger Se-Sn bonds, which results in an increase in T_{g} [22,23].

In this study, the AKTS software package was used to calculate the activation energy of crystallisation. The AKTS software was based on optimising for the baseline correction while simultaneously applying isoconversional techniques; a full description of the applied AKTS software is discussed in greater detail elsewhere [24].

With the exception of the sample with 0 at% of Sn, the asymmetric shape of the experimental peaks, as clearly observed for the sample with 7.5 at% of Sn, implies that the peaks correspond to complex processes involving more than one step. However, the equation describing the behaviour for a single-step process can give a sufficient kinetic representation of a multi-step process.

Fig. 2 shows the dependence of E_α on the reaction progress, α, accomplished by applying four isoconversional methods of Friedman Eq. 4, FWO Eq. 8, and Vyazovkin Eq. 9, which computed by the tow temperature integrals Eqs. 10 and 11.
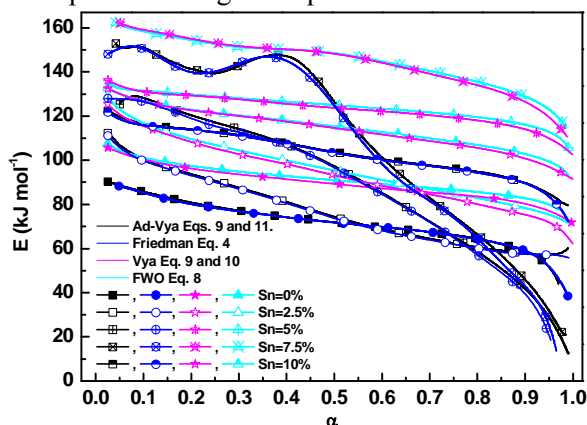

Fig. 2. Dependence of the activation energy for crystallisation, E_α, on the reaction progress, α.

As expected, the results accomplished by the Vya (temperature integral) and FWO methods are in good agreement and reveal almost the same values of E_α. Furthermore, the Ad-Vya (advanced temperature integral) and Friedman methods reveal as well the same values of E_α. This gives a clear indication that the temperature integral approximation results in inaccurate values of E_α.
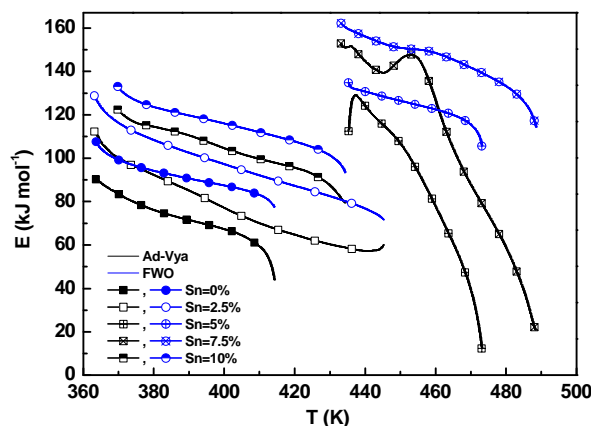

Fig. 3. Dependence of the activation energy for crystallisation, E_α, on the temperature.

The results acquired by the FWO and Vya methods indicate that the activation energy for crystallization, E_α, is mainly independent of the value of α, with some exceptions in the final stage of crystallisation. The results obtained using the Friedman and Ad-Vya methods exhibit a very strong variation of E_α with α for the 5 and 7.5 at% Sn samples. The variation of T versus α is shown in Fig. 3. For the 7.5 at% Sn sample, the peak at approximately 453 K suggests the occurrence of parallel reactions.

Based on the obtained linear relationship between $\left(1/T_{\mathrm{P}}\right)$ and $\left(\ln\left(\beta/T_{\mathrm{P}}\right)\right)$, the ASTM E698 method was used to calculate the activation energy; the results obtained alongside some other kinetic parameters are summarised in Table 1. In addition, Fig. 4 shows the variation of the activation energy obtained from the ASTM E698 method with Se concentration. To change the material from a stable phase into another phase the activation energy, which represents the energy barrier must be overcome.
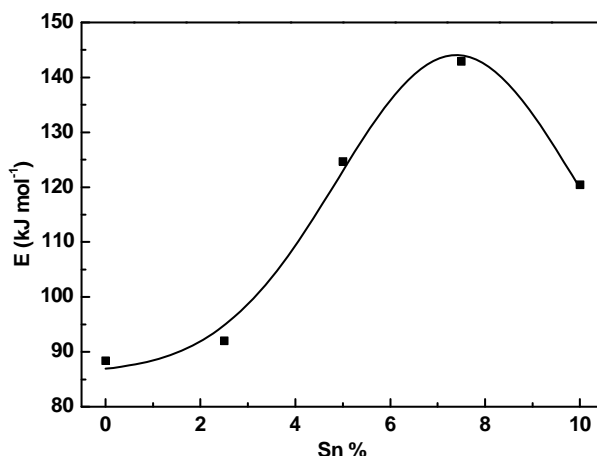

Fig. 4. The variation of the activation energy, E, as determined by the ASTM E698 method, with Sn concentration, where the solid line represents a Gaussian fit.

Thus, according to the obtained values of the activation energy of crystallisation, it is immediately obvious that this energy barrier increases with Se concentration. The pre-exponential factor, A, was calculated from the expression given in ASTM E698 [25-27]:

$$A = \beta\left(\frac{E}{RT_P^2}\right)\exp\left(\frac{E}{RT_P}\right) \qquad (15)$$

To determine the crystallisation mechanism, Matusita and Sakka [28,29] suggested an equation that is applicable for non-isothermal crystallisation and is given by:

$$\ln\left[-\ln\left(1-\alpha\right)\right] = -n\ln\beta - 1.052\frac{mE}{RT} + \text{constant}, \qquad (16)$$

where m and n are the constants related to the crystallisation mechanism, m is an integer that depends on the dimensionality of the crystal, and n is the Avrami exponent that depends on the nucleation process. When the nuclei formed during the constant-rate heating dominate, $n = m + 1$, and when nuclei formed during any heat treatment prior to the thermal analysis are dominant, $n = m$. In this work, $n = m$ because before each experimental run the samples were pre-annealed for a period of time at a temperature below the glass transition temperature, T_g, hence certifying that the nucleation sites were saturated [30].

Thus, to obtain E, the above equation (Eq. 16) was used at different heating rates, β_i. The plot of $\ln\left[-\ln\left(1-\alpha\right)\right]$ versus $10^3/T$ yields straight lines. Therefore, the Avrami exponent n is [30]:

$$\frac{d\left\{\ln\left[-\ln\left(1-\alpha\right)\right]\right\}}{d\left(\ln\beta\right)}\Bigg|_T = -n. \qquad (17)$$

The calculated values of n were not integers, with the exception of the 5 at% Sn sample $\left(n = 4\right)$, as shown in Table 1. The lack of integer values of n indicates that the crystallisation

occurs via different mechanisms. The average values of the kinetic exponent n indicate predominantly two-dimensional growth $(n = 2.41)$ for the binary system $Se_{90}Te_{10}$, while the results indicate one-dimensional growth $(n = 1.22$ and $1.24)$ for the two systems with 2.5 and 10 at% of Sn. The high value of the Avrami exponent $(n = 5.96)$ for the composition $Se_{82.5}Te_{10}Sn_{7.5}$ indicates a very high nucleation rate with three-dimensional growth. Normally, n should not exceed 4; however, high values of n $(n = 5.54)$ have been reported for the system $Se_{79}Te_{15}Sn_6$ [3]. Fig. 5 shows the variation of the activation energy for crystallisation with the heating rate obtained from the Matusita and Sakka method. The result indicates a significant dependence of the activation energy on the heating rate.
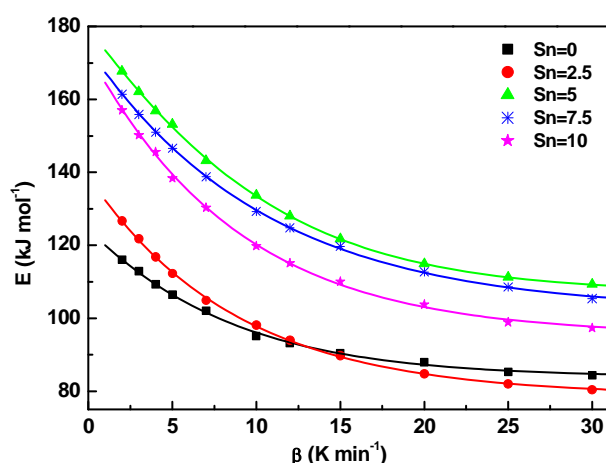

Fig. 5 The variation of the activation energy, E, with the heating rate, β, as determined by the Matusita and Sakka method.

Table 1. Comparison of kinetic parameters for amorphous $Se_{90-x}Te_{10}Sn_x$ at various Sn contents.

Sample	$\beta = 5\ K\ min^{-1}$		ASTM Activation Energy kJ mol^{-1}	A sec^{-1}	n from Matusita and Sakka Eq. 17	n from the reaction model
	T_g (K)	T_P (K)				
$Se_{90}Te_{10}$	327.7	377	88.4	8.7×10^9	2.41	2
$Se_{87.5}Te_{10}Sn_{2.5}$	328.5	393.4	92	1.02×10^{10}	1.22	1.2, $\alpha < 0.6$ 1.5, $\alpha > 0.6$
$Se_{85}Te_{10}Sn_5$	352.6	453.8	124.7	2.25×10^{12}	4	4
$Se_{82.5}Te_{10}Sn_{7.5}$	355.8	456.1	142.9	1.66×10^{14}	5.96	2, $\alpha < 0.6$ 5.96, $\alpha > 0.6$
$Se_{80}Te_{10}Sn_{10}$	335.6	388.3	120.4	1.23×10^{14}	1.24	1.5, $\alpha < 0.7$ 1.2, $\alpha > 0.7$

More often, the integral of the reaction model, $g(\alpha)$, is used to explain the kinetics of phase change in solids. More precisely, the kinetic models listed in Table 2 can be used to explain the crystallisation process. However, $g(\alpha)$, is given for isothermal kinetics as [31,32]:

$$g(\alpha) = A\frac{t}{t_\alpha}, \qquad (18)$$

Where A is a calculated constant dependent on the form of the function $g(\alpha)$ and t_α is the time required to reach a specific conversion, e.g., $\alpha = 0.5$. Eq. 17 is independent of the kinetic rate

constants and is dimensionless. In non-isothermal studies when the reduced activation energy (E/RT) comes close to infinity the reaction progress comes close to $\alpha = 0.632$ at the corresponding temperature and the constant $A = 1$, so the reaction progress was chosen to be $\alpha = 0.632$ [33].

The kinetic parameters calculated from the non-isothermal experiments enable the prediction of the reaction progress, α, for the other mode, such as isothermal [34-38]. For the samples under investigation and from the results of advanced temperature integral, the prediction of the isothermal reaction progress is shown in Fig. 6. The temperatures indicated in the figure are the peak temperatures resulting from a heating rate of 5 K min^{-1}. Fig. 7 shows the calculated values of the reaction model, $g(\alpha)$, using Eq. 18 with $\alpha = 0.632$, along with the theoretical plots for different Mechanism (Table 2).
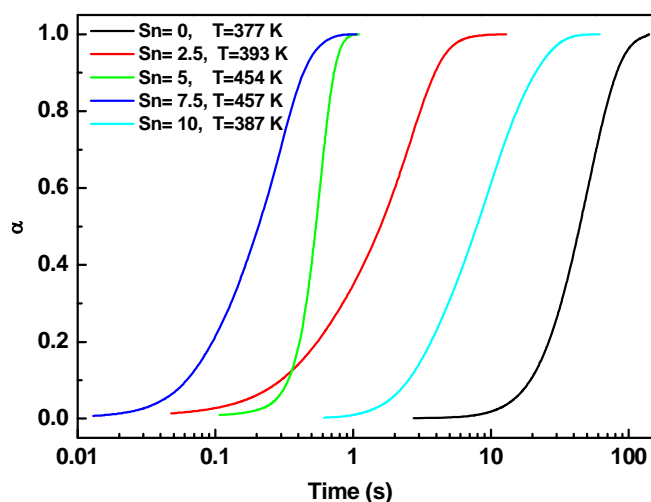

Fig. 6. Prediction of the reaction progress of the crystallisation of the examined samples as a function of time under isothermal conditions. The temperatures indicated in the figure are the peak temperatures corresponding to a heating rate of 5 K min^{-1}.
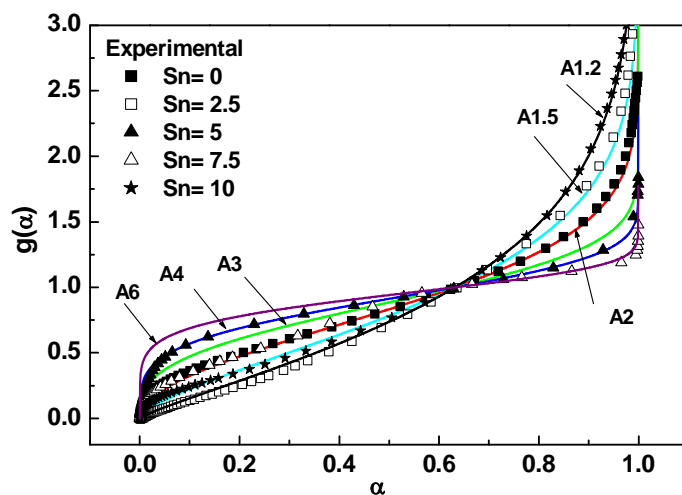

Fig. 7. The variation of the reduced reaction model, $g(\alpha)$, versus the reaction progress, α, derived from the reduced reaction model analysis (the solid line was calculated from the various theoretical models listed in Table 2).

Table 2. Common solid state reaction models used to describe the crystallization process.

Model Notation	$g(\alpha)$	Mechanism
A1.5	$\left[-\ln(1-\alpha)\right]^{2/3}$	Avrami-Erofeev, $n = 1.5$
A2	$\left[-\ln(1-\alpha)\right]^{1/2}$	Avrami-Erofeev, $n = 2$
A3	$\left[-\ln(1-\alpha)\right]^{1/3}$	Avrami-Erofeev, $n = 3$
A4	$\left[-\ln(1-\alpha)\right]^{1/4}$	Avrami-Erofeev, $n = 4$

To gain information about the change of the reaction mechanisms through the route of crystallization, the obtained results were judged against those derived from the theoretical models. It is immediately obvious from Fig. 7 that the reactions follow an Avrami-Erofeev mechanism. Obviously, the investigation for solid-state reaction models indicates that the mechanism varies with Sn concentration. The reaction mechanism was determined to be A2 for the 0 at% Sn base sample, followed by a change to A1.5 as the Sn concentration increased to 2.5 at% for $\alpha > 0.6$. Additionally, the mechanism tended to be A1.2 for $\alpha < 0.6$ and A4 for the 5 at% Sn sample. The 7.5 at% Sn sample exhibited anomalous values of the Avrami-Erofeev mechanism; it was A2 at low values of the reaction progress $(\alpha < 0.6)$, subsequently shifting to a value of A>4 for $\alpha > 0.6$. However, the $Se_{80}Te_{10}Sn_{10}$ alloy was associated with the A1.5 mechanism at $\alpha < 0.7$ but changed to A1.2 at higher values of the reaction progress. The representation of the $Se_{82.5}Te_{10}Sn_{7.5}$ sample should be performed by peak deconvolution, which will be examined in a separate study.

3.2 Specific heat capacity studies

It is instructive to discuss some aspects related to the specific heat capacity. A typical MDSC heating scan is shown in Fig. 8, which demonstrates the non-reversing, reversing, and modulated heat flow.
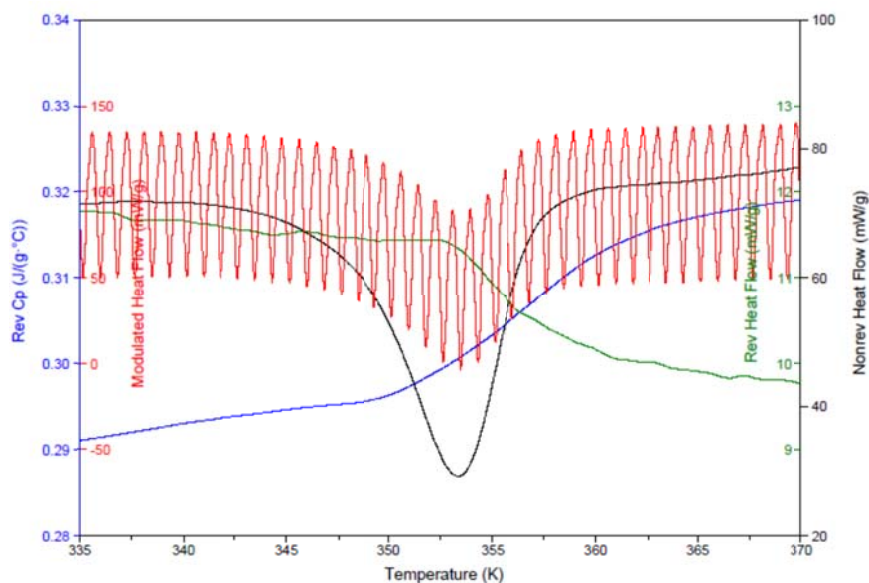

Fig. 8. Typical example of the components of the MDSC scans for glassy $Se_{90-x}Te_{10}Sn_x$ alloys.

The figure shows the reversing specific heat capacity in the region of the glass transition for the 5% Sn sample. Using Eq. (13), the specific heat capacity, c_P, was evaluated, and the results are shown in Fig. 9.
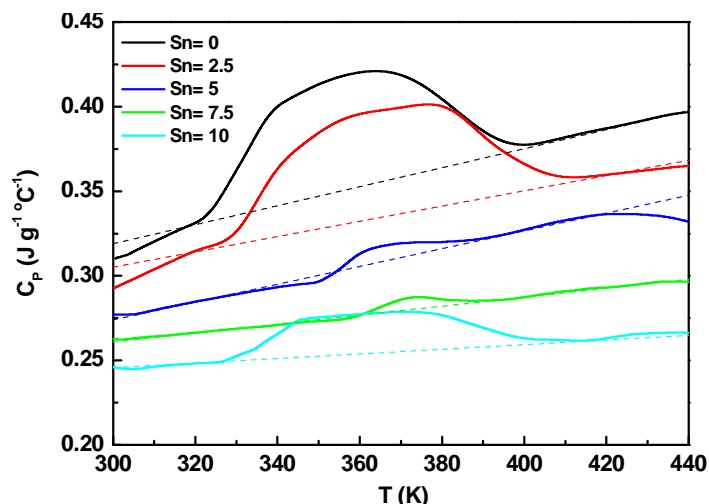

Fig. 9. Temperature dependence of the specific heat capacity, c_P, in glassy $Se_{90-x}Te_{10}Sn_x$ alloys.

The 0 and 2.5% Sn samples have distinctly high specific heat values compared with those of the 5, 7.5, and 10% Sn samples; nevertheless, all of the values remained within a narrow range. As expected, due to the increased molecular mobility, the c_P value increased with temperature. Though, the c_P value increased significantly with increasing temperature and exhibited a maximum at the glass transition temperature (S shape). Ahead of the glass transition region, the value of c_P reached a stable value that was clearly higher than that of c_P before the glass transition region. If these S-shaped peaks are extracted and limited to correspond to temperatures below the melting point, the heat capacities for all samples can be fitted to a straight line. The average of the variation of c_P with temperature for all the samples can be given as $\left(c_P = 0.16 + 3.88 \times 10^{-4} T\right)$, as represented in Fig. 9. The known anharmonic involvement in the structural relaxation leads to an increase in c_P above the glass transition temperature T_g [39,40].

According to the Maslyuk model [41] proposed for describing the maximum heat capacities of chalcogenide glasses, for the chalcogenide glasses the glass-liquid transition can be described as a transition from a structured amorphous state (represents glass specific heat c_{Pg}) to the liquid homogenised state (represents equilibrium liquid specific heat c_{Pe}). This is because the heat capacity maximum depends on the energy build-up capacity of the structural groups. From Table 3, it is clear that both c_{Pe} and c_{Pg} and their difference, Δc_P, are significantly decreased after the incorporation of Sn in the binary $Se_{90}Te_{10}$ alloy at the cost of Se. This behaviour can be described in terms of the values of the specific heats c_P of Se and Sn and their atomic weights. The room-temperature specific heat c_P of Se $\left(0.33 \text{ Jg}^{-1}\,^{\circ}\text{C}^{-1}\right)$ is higher than that of Sn $\left(0.24 \text{ Jg}^{-1}\,^{\circ}\text{C}^{-1}\right)$. On the contrary, the atomic weight of Se (78.96 g mol^{-1}) is less than that of Sn (118.71 g mol^{-1}). In chalcogenide glasses some thermally induced structural relaxation is known to occur during the glass transition. As a result, more specific heat is required to induce structural rearrangements with the increase in the atomic weight of the binary alloys, which is most likely

the reason for the decrease in the c_p values with the increase in the Sn content. A similar behaviour was observed in another glassy system by other researchers [40].

Table 3. values of both c_{Pe}, c_{Pg} and their difference Δc_p for amorphous $Se_{90-x}Te_{10}Sn_x$ at various Sn contents.

Sample	$c_{Pe}\ \left(Jg^{-1}\,{}^\circ C^{-1}\right)$	$c_{Pg}\ \left(Jg^{-1}\,{}^\circ C^{-1}\right)$	$\Delta c_P\ \left(Jg^{-1}\,{}^\circ C^{-1}\right)$
$Se_{90}Te_{10}$	0.329	0.379	0.05
$Se_{87.5}Te_{10}Sn_{2.5}$	0.315	0.360	0.045
$Se_{85}Te_{10}Sn_5$	0.296	0.325	0.029
$Se_{82.5}Te_{10}Sn_{7.5}$	0.274	0.288	0.014
$Se_{80}Te_{10}Sn_{10}$	0.249	0.261	0.012

3.3 Raman scattering studies

The results of the Raman scattering investigation of amorphous $Se_{90-x}Te_{10}Sn_x$ at room temperature are shown in Fig. 10.
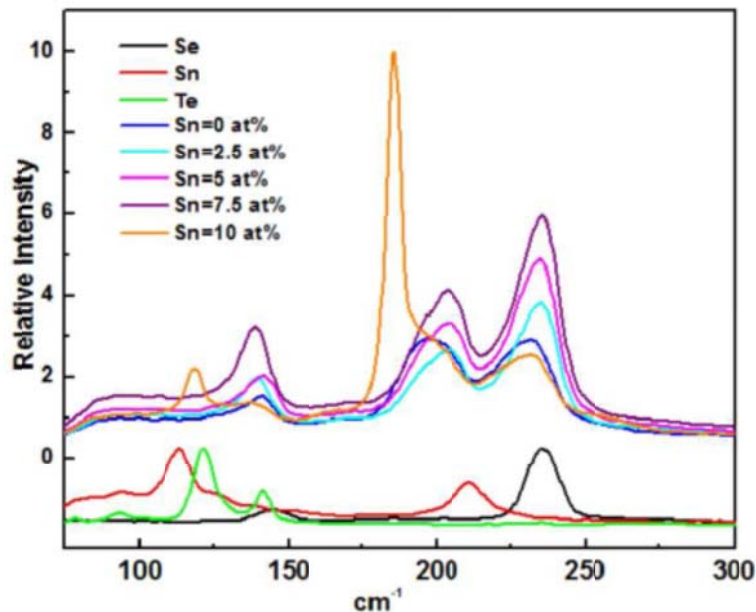

Fig. 10. Raman spectra of amorphous $Se_{90-x}Te_{10}Sn_x$ and the starting materials (Se, Te, and Sn).

Note that the change in the Sn concentration varies the intensity and width of the Raman peak. However, because the relative intensities of the Raman peaks in the same trace provide a unique indication of the composition dependence of the molecular structure, a relative intensity scale was employed for the alloy compositions. The Raman spectra for the starting materials (Se, Te, and Sn) are also represented in the bottom of Fig. 10, but the intensities of the signals were normalised to one. Figs. 10 demonstrate that a spectral change occurs following the addition of 10 at% of Sn into the $Se_{90}Te_{10}$ glass. First, in the 123-154-cm^{-1} region, a small prominence at approximately 140 cm^{-1} can be observed for the 0, 2.5, 5, and 7.5 at% Sn samples. Second, a clear, strong, and broad spectrum is present in the 178-260-cm^{-1} region. This spectrum divides into two dominating peaks at approximately 203 cm^{-1} and 234 cm^{-1}. Third, a strong, well-defined, and narrow peak at 186 cm^{-1} is present with the increasing content of Sn up to 10 at%, along with a small peak at 119 cm^{-1}.

The data shown in Fig. 10 indicate that the dominant trigonal Se spectral lines are located at approximately 235 and 144 cm^{-1}, which is in good agreement with the results of other researchers [42,43]. Fig. 10 also reveals that the addition of Te to Se introduces a new spectral feature, namely the appearance of a very wide spectrum with two peaks at approximately 232 and

198 cm^{-1}; these same features were observed by other researchers [44,45]. The positions of this spectrum shift slightly to approximately 235 and 205 cm^{-1} with increasing Sn content. The weak band attributed to trigonal Se at 144 cm^{-1} exhibits a shift to 141 cm^{-1} in the Se-Te system. A notable change in the Raman peak occurs at a Sn concentration of 10 at%. This notable change was previously observed for the Sn_xSb_5–Se_{95-x} system with the same Sn concentration of 10 at% [44]. The peak at 185 cm^{-1} was previously reported for tetrahedral $SnSe_4$ [46].

A comparison of the Raman scattering results with the XRD patterns shown in Fig. 11 indicates that for low concentrations of Sn of 5 at% or less, the main peaks are attributed to Se hexagonal (101) [JCPDS file 06-0362]; the medium-intensity peaks are attributed to selenium telluride ($Se_{5.95}Te_{1.05}$), as is evident from Fig. 11 for the peaks of SeTe (202) and (114) [JCPDS file 87-2414], and the remaining low-intensity peaks are attributed to SnSe (111) and (501) [JCPDS file 89-0232]. For higher Sn concentrations, e.g., 7.5 at% Sn, the dominant strong peaks are associated with $Se_{5.95}Te_{1.05}$, as is evident from Fig. 11 for the peaks SeTe (400), (114), (242), and (234) [JCPDS file 87-2414]. However, as in the Raman spectra, new peaks were found for the 10 at% sample; it is believed that these peaks are attributed to the formation of $SnSe_2$. The XRD patterns in Fig. 11 support this hypothesis by presenting the peaks for $SnSe_2$ (001), (101), (102), and (004) [JCPDS file 23-0602].
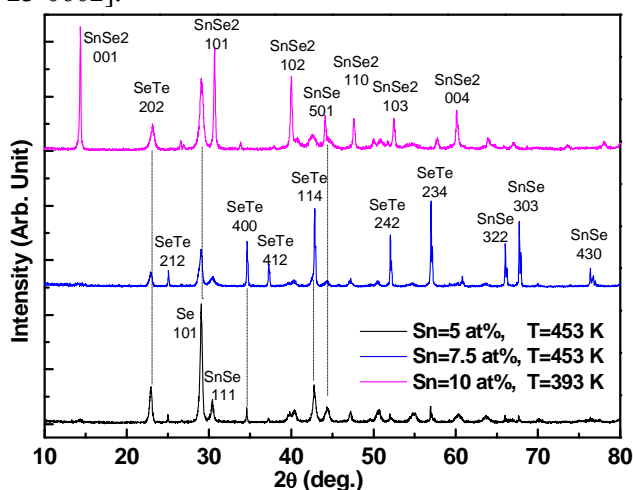

Fig. 11. XRD patterns of the $Se_{90-x}Te_{10}Sn_x$ sample. The temperatures indicated in the figure represent the data collection temperatures.

The results of the Raman scattering and XRD studies help explain the structure of the Se–Te–Sn system. In both Se and Te only the two odd electrons in the outer electronic shell $s^2 p_x^2 p_y^1 p_z^1$ are concerned in the formation of strong covalent bonds to build the inorganic polymeric hexagonal system. However, for the formation of the solids the main structural building unit is an infinite long chain of Se atoms, with a coordination number of 2. Furthermore, small amounts of cross-linking atoms of Te were added to these selenium chains, with a coordination number of 2. The interchain cohesion bonding in Se and Te are the Van der Waals and the metallic bonding, respectively [47].

The addition of Sn to the Se-Te system modifies it and results in a coordination number of 4 in the structure, but it still results in a glass structure. However, these amounts should be less than that required for $SnSe_2$. Thus, the probability of bond formation shows the least existence of bonds like Se-Se, Se-Te, and Sn-Se at concentrations of $Sn \leq 7.5$ at%. By increasing the Sn concentration up to 10 at%, the structural units of $SnSe_4$ tetrahedrons will be developed, which is assumed to be the basic structural unit of $SnSe_2$ [46,48]. These units spread out among the Se chains and result in a Se3–Sn–Se–Se–Te–Se glass structure.

Finally, the results of all the experimental runs indicate a remarkable change occurring at a Sn concentration of 10 at%.

4. Conclusion

MDSC studies were performed on $Se_{90-x}Te_{10}Sn_x$ glasses. The activation energies of crystallisation, E_α, were estimated by applying three isoconversional methods. The results acquired by the Flynn-Wall-Ozawa method indicate that the activation energy for crystallisation, E_α, is mainly independent of the value of α. The Friedman and advanced Vyazovkin methods indicates a very strong variation of E_α with α for the 5 and 7.5% Sn samples. Based on the ASTM E698 analysis, the effect of Sn content on the activation energy for crystallisation exhibits an increase followed by a decrease for Sn > 7.5 at%. The integral form of the reaction model, $g(\alpha)$, was determined to change with increasing Sn content.

The values of c_{Pe} and c_{Pg} were determined to decrease after the incorporation of Sn into the binary $Se_{90}Te_{10}$ alloy at the cost of Se. The decreasing sequence of Δc_P values in the binary alloys is explained in terms of their mean atomic masses.

The Raman spectra together with the XRD data indicate the possible existence of the Se-Se, Se-Te, Sn-Se, and $SnSe_2$ bonds.

Acknowledgements

References

[1] L.C. Thomas, TA Instruments Publication, No. TA 226 and No. TA 227, http://www.tainst.com.

[2] B.H. Sharmila, J.T. Devaraju, S.A. Asokan, J. Non-Crystalline Solids **326&327,** 154 (2003).

[3] B.S. Patial, N. Thakur, S.K. Tripathi, J. Therm. Anal. Calorim. **106,** 845 (2011). A.A. Joraid, Thermochim. Acta **456**, 1 (2007).

[4] O.A. Lafi, M.M.A. Imran, J. Alloys Compd. **509**, 5090 (2011).

[5] B.S. Patial, N. Thakur, S.K. Tripathi, Thermochim. Acta **513**, 1 (2011).

[6] S. Kumar, K. Singh, Thermochim. Acta 528 (2012) 32.

[7] AKTS-Thermokinetics Version 3.64 http://www.akts.com (AKTS-Thermokinetics software) 2013.

[8] S. Vyazovkin, A.K. Burnham, J.M. Criado, L.A. Pérez-Maqueda, C. Popescu, N. Sbirrazzuoli, Thermochim. Acta **520**, 1 (2011).

[9] J. Farjas, P. Roura, J. Therm. Anal. Calorim. **105**, 757 (2011).

[10] H.L. Friedman, J. Polym. Sci. C **6**, 183 (1964).

[11] T.A. Ozawa, Bull. Chem. Soc. Jpn. **38**, 1881 (1965).

[12] J.H. Flynn, L.A. Wall, J. Res. Natl. Bur. Stand. Sect. A **70**, 487 (1966).

[13] S. Vyazovkin, J. Comput. Chem. **18**, 393 (1997).

[14] S. Vyazovkin, J. Comput. Chem. **22**, 178 (2001).

[15] P. Budrugeac, J. Therm. Anal. Cal. **68**, 131 (2002).

[16] C.D. Doyle, J. Appl. Polym. Sci. **6**, 639 (1962).

[17] ASTM E698 - 11. http://www.astm.org/Standards/E698.htm

[18] A. Iliyas, K. Hawboldt F. Khan, J. Hazardous Materials **178**, 814 (2010).

[19] J.E.K. Schawe, T. Hutter C. Heitz, I. Alig, D. Lellinger, Thermochim. Acta 446, 147 (2006).

[20] A.A. Joraid, Thermochim. Acta **436**, 78 (2005).

[21] G. Kaur, T. Komatsu, R. Thangaraj, J. Mater. Sci. 35 (2000) 903.

[22] R. Kumar, P. Sharma, P.B. Barman, V. Sharma, S.C. Katyal, V.S. Rangra, J. Therm. Anal. Calorim. **110**, 1053 (2012).

[23] B. Roduit, B. AKTS AG Advanced Kinetics and Technology Solutions, Analysis report. http://www.akts.com.

[24] Y.S. Li, M.S. Li, F.C. Chang, J. Polym. Sci. Part A:Polym. Chem. **37**, 3614 (1999).

[25] R. Turcotte, M. Vachon, Q.S.M. Kwok, R. Wang, D.E.G. Jones, Thermochim. Acta **433**, 105 (2005).

[26] Q. Wang, L. Wang, X. Zhang, Z. Mi, J. Hazard. Mater. **172**, 1659 (2009).

[27] K. Matusita, S. Sakka, Phys. Chem. Glass **20**, 81 (1979).

[28] K. Matusita, S. Sakka, Bull. Inst. Chem. Res. Kyoto Univ. **59**, 159 (1981).

[29] A.A. Joraid, S.N. Alamri, A.A. Abu-Sehly, J. Non-Cryst. Solids **354**, 3380 (2008).

[30] A.C. Lua, J. Su, Polym. Degrad. Stabil. **91**, 144 (2006).

[31] S. Majumdar, I.G. Sharma, A.C. Bidaye, A.K. Suri, Thermochim. Acta **473**, 45 (2008).

[32] A.A. Joraid, S.N. Alamri, A.A. Abu-Sehly, S.Y. Al-Raqa, P.O. Shipman, P.R. Shipley, A.S. Abd-El-Aziz, Thermochim. Acta 515 (2011) 38.

[33] B. Roduit, C. Borgeat, B. Berger, P. Folly, B. Alonso, J.N. Aebischer, F. Stoessel, J. Therm. Anal. Cal. 80 (2005) 229.

[34] B. Roduit, L. Xia, P. Folly, B. Berger, J. Mathieu, A. Sarbach, H. Andres, M. Ramin, B. Vogelsanger, D. Spitzer, H. Moulard, D. Dilhan, J. Therm. Anal. Cal. **93,** 143 (2008).

[35] B. Roduit, W. Dermaut, A. Lunghi, P. Folly, B. Berger, A. Sarbach, J. Therm. Anal. Cal. **93** 163 (2008).

[36] A.K. Burnham, L.N. Dinh, J. Therm. Anal. Cal. **89**, 479 (2007).

[37] H. Eloussifi, J. Farjas, P. Roura, M. Dammak, J. Therm. Anal. Cal. **108**, 597 (2012).

[38] A. Sharma, H. Kumar, N. Mehta, Materials Letters **86**, 54 (2012).

[39] S. Saraswat, S. Kushwaha, J. Therm. Anal. Cal. **96**, 923 (2009).

[40] V. Maslyuk, J. Non-Cryst. Solids **212**, 80 (1997).

[41] K. Nagata, K. Ishibashi, Y. Miyamoto, Jpn. J. Appl. Phys. **20**, 463 (1981).

[42] V.S. Minaev, S.P. Timoshenkova, V.V. Kalugina, J. Optoelectron. Adv. Mater. **7**, 1717 (2005).

[43] A. Ward, J. Phys. Chem. **74**, 4110 (1970).

[44] R. Geick, E.F. Steigmeier, H. Auserset, Phys. Stat. Sol. (b) **54**, 623 (1972).

[45] A.B. Adam, J. King Saud University (Science) **21**, 93 (2009).

[46] B. Bureau, C. Boussard-Pledel, P. Lucas, X. Zhang, J. Lucas, Molecules **14**, 4337 (2009).

[47] R. Kumar, P. Sharma, S.C. Katyal, P. Sharma, V.S. Rangra, J. Appl. Phys. **110**, 013505 (2011).